RSC Advances

ROYAL SOCIETY OF CHEMISTRY

www.rsc.org/advances

RSC Advances

Cite this: DOI: 10.1039/c0xx00000x

ARTICLE TYPE

www.rsc.org/xxxxxx

Effect of niobium doping on the microstructure and electrochemical properties of lithium-rich layered $Li[Li_{0.2}Ni_{0.2}Mn_{0.6}]O_2$ as cathode materials for lithium ion batteries

Xiangjun Li, Hongxing Xin,* Yongfei Liu, Di Li, Xueqin Yuan, Xiaoying Qin*

Received (in XXX, XXX) Xth XXXXXXXXX 20XX, Accepted Xth XXXXXXXXX 20XX
DOI: 10.1039/b000000x

The niobium-doped lithium-rich layered cathode materials, $Li[Li_{0.2}Ni_{0.2}Mn_{0.6-x}Nb_x]O_2$ (x = 0, 0.02, 0.04, and 0.06), were prepared and the effects of Nb doping on the microstructure and electrochemical properties were investigated. Upon Nb doping, the layered α-$NaFeO_2$ structure is maintained but with an expanded interlayer spacing and the electrochemical properties are significantly enhanced. In particular, the sample with x = 0.04 delivers a large reversible discharge capacity of 254 mAh•g^{-1} at 0.1C rate with a high capacity retention rate of 92.3% after 100 cycles. Furthermore, it delivers 198 mAh•g^{-1} at 1C rate, much larger than that of the undoped sample (125 mAh•g^{-1}). Capacity differential results reveal that strong Nb–O bond can stabilize the material structure and thus lead to a stable cycling performance. Electrochemical impedance spectroscopy (EIS) analysis shows that Nb doping can decrease the whole cell impedance and expand the Li^+ diffusion path in the lithium-rich layered cathode materials, resulting in the excellent rate capability.

1. Introduction

In the past decade, lithium-ion batteries have been developed steadily as the portable energy storage devices, due to their higher energy and power density per unit as compared with other rechargeable battery systems. With the rise of electric enterprises, such as the Tesla motor, etc., the searching for safe and economical cathode materials with elevated voltage, high capacity and good cycle performance has become one of the focuses in recent years. Among the reported cathode materials, the lithium-rich (Li-rich) solid solution cathode materials between layered $Li[Li_{1/3}Mn_{2/3}]O_2$ (commonly written as Li_2MnO_3) and $LiMO_2$ (M = Mn, Co, Ni)[1-12] have become attractive in recent years as they deliver a high capacity of around 250 mAh•g^{-1}. Meanwhile, they have the advantages of reduced cost and improved safety as compared to the conventional $LiCoO_2$ cathode.

Nevertheless, these Li-rich material has some disadvantages, such as the large-capacity loss during the initial charge/discharge cycle, poor rate capability and the continuous voltage fading.[13, 14] To solve these problems, various attempts has been made, e.g. surface modification with metal oxides,[11, 15-18] shortening the lithium-ion diffusion pathways by reducing the particle size,[19,20] and substituting a small amount of doping ions at the transition metal sites.[21-25] It has been widely reported that the doping of fixed-valence-state elements, such as Al^{3+},[26] Cr^{3+},[22] Co^{3+},[23] Ru^{4+},[9] and F^-,[25,27] etc., could substantially improve the electrochemical performance of the Li-rich layered cathode materials.

It is known that the poor rate capability of Li-rich cathode could be related to the inferior electronic conductivity of Li_2MnO_3 component.[3] On the other hand, part of Li_2MnO_3 component could transform from the layered structure to the spinel-like structure at the end of the first discharge process.[28] To overcome these drawbacks, element doping has been reported to be an effective way by improving their thermal and structural stability.[29] Element doping could prevent these structure transformations and enhance the diffusivity of electrons and lithium ions in the cathode materials.

According to Lange's Handbook of Chemistry, [30] the bond dissociation energy of Nb–O (ΔHf(Nb-O)=753 kJ•mol^{-1}) is stronger than that of Mn–O (ΔHf(Mn-O)=402 kJ•mol^{-1}), which could contribute to the stability of the bulk layered structure. Meanwhile, the doped Nb^{5+} ions are expected to expand the Li^+ channel in the layered structure due to their larger radius (0.69 Å) as compared to Mn^{4+} ions (0.53 Å).[31] As far as we know, however, there is lack of studies on the electrochemical performance of Li-rich cathode materials doped by niobium. Thus, niobium ion (Nb^{5+}) is selected as a dopant to substitute Mn^{4+} in the layered Li-rich materials, $Li[Li_{0.2}Ni_{0.2}Mn_{0.6}]O_2$ (or $0.5Li_2MnO_3$•$0.5LiMn_{0.5}Ni_{0.5}O_2$).

In the present work, $Li[Li_{0.2}Ni_{0.2}Mn_{0.6-x}Nb_x]O_2$ (x = 0, 0.02,

[a] *Key Laboratory of Materials Physics, Institute of Solid State Physics, Chinese Academy of Sciences, Hefei 230031, PR China. E-mail : xinhongxing@issp.ac.cn Tel: +86-551-65591036 Fax:+86-551-65591434.*

0.04, and 0.06) compounds were prepared by a solid-state reaction, and the effects of niobium doping on the microstructure, and electrochemical behaviour of the materials were investigated. The mechanisms for the improved cycling performance and rate capability were also discussed.

2. Experimental

2.1 Synthesis of $Li[Li_{0.2}Ni_{0.2}Mn_{0.6-x}Nb_x]O_2$

$Li[Li_{0.2}Ni_{0.2}Mn_{0.6-x}Nb_x]O_2$ (x = 0, 0.02, 0.04, and 0.06) materials were synthesized by a two-step process. Firstly, a carbonate precursor $Ni_{0.2}Mn_{0.6-x}CO_3$ was prepared by co-precipitation of 2 M aqueous solution of Ni and Mn sulphate (Ni:Mn = (0.2:0.6-x) with the 2 M solution of Na_2CO_3 at the temperature of 55 ºC. The pH was adjusted to approximately 8.0 by ammonium hydroxide (NH_4OH) solution. The obtained $Ni_{0.2}Mn_{0.6-x}CO_3$ was washed with deionized water for several times and subsequently dried in a vacuum oven. Secondly, the carbonate $Ni_{0.2}Mn_{0.6-x}CO_3$ was completely mixed with Li_2CO_3 and Nb_2O_5 according to the stoichiometric ratio, and then annealed in air at 500 ºC for 5 h to decompose the carbonate precursors. The as-prepared powders were pressed into pellets. Finally, these pellets were sintered at 850 ºC for 12 h in air and ground into powders. In addition, a 3 wt.% excess of Li_2CO_3 was added to compensate for lithium loss during the high temperature calcination.

2.2 Microstructure characterization

The phase structures of the as-synthesized products were examined by powder X-ray diffraction (XRD) (Philips-X PERT PRO diffractometer) using Cu Kα radiation. The morphology of the as-synthesized products was examined by Field emission scanning electron microscopy (FE-SEM, SIRION 200). In addition, X-ray photoelectron spectroscopy (XPS, ESCALAB 250, Thermo-VG Scientific) was performed to compare the compositions and ionic environments of the undoped and doped samples using an Al monochromatic X-ray (hν =1486.6 eV) source.

2.3 Electrochemical measurements

The electrodes were fabricated from a mixture of active materials, super-P carbon black and polyvinylidene difluoride (PVDF) in the ratio of 85:10:5 (wt.%). The PVDF was dissolved in N-methylpyrro-lidinone (NMP), and then the active material and Super-P carbon black were added. After homogenization, the slurry was evacuated to remove residual air. The slurry was coated on a thin aluminium foil (20 μm thick) and dried in a vacuum oven. The electrode was pressed and punched into round disks with 15 mm in diameter. The thickness of the electrodes was about 40-80 μm (mass loading of the active material 2.2-4.5 mg/cm^2). Standard 2032 coin cells were assembled in a dry Ar-filled glove box to test the electrochemical properties of the cathode materials. Lithium metal foils were used as the counter electrode, and 1.0 mol/L $LiPF_6$/(EC:EMC:DEC = 1:1:1) as the electrolyte. After aging for 10 h to ensure thorough wetting of the electrolyte, the coin cell was charged and discharged at room temperature within the range of 4.8~2.0 V(vs. Li^+/Li). The electrochemical impedance spectroscopy (EIS) of the coin cell was evaluated in the frequency range from 0.01 Hz to 100 kHz at Zahner Zennium electrochemistry workstation. The amplitude of the AC signal was 5 mV.

3. Results and discussion

3.1 Microstructure characterization

XRD patterns of $Li[Li_{0.2}Ni_{0.2}Mn_{0.6-x}Nb_xO_2$ (x = 0, 0.02, 0.04, and 0.06) are shown in Fig. 1. Diffraction pattern of the undoped sample can be identified as a layered α-$NaFeO_2$ structure with space group R $\bar{3}$ m. Meanwhile, the splitting of [(1 0 8), (1 1 0)] and [(0 0 6), (1 0 2)] peaks is observed without any impurity reflections, indicating the highly ordered layered structure. The weak superstructure reflections observed around 20~25° (2θ) are known as the characteristic of a Li_2MnO_3-type structure with $LiMn_6$ (or Ni-substituted) cation ordering in the transition metal layers.[32, 33] It can be indexed to the Li_2MnO_3 (PDF#01-081-1953) with monoclinic unit cell and space group C2/m.[34] In the doped samples, the main patterns are also consistent with the undoped layered structure. However, some minor residual peaks (as marked by asterisks) appear with the increase of the doping amount. For instance, in the sample with x = 0.06, distinct peaks emerge, which can be indexed as Li_3NbO_4 phase (PDF#00-016-0459) and Nb_2O_5 phase (PDF#00-070-2679). These impurities should originate from excess doping of niobium.

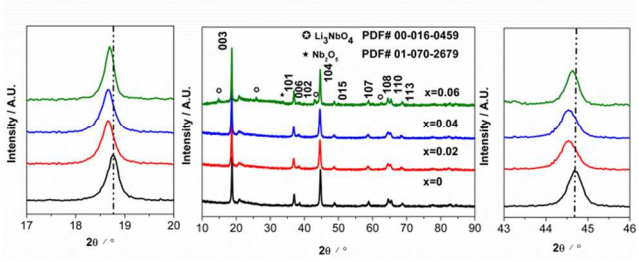

Fig.1 XRD patterns of $Li[Li_{0.2}Ni_{0.2}Mn_{0.6-x}Nb_x]O_2$ (x = 0, 0.02, 0.04, 0.06) and the magnified view of peak (003)&(104).

Lattice constants are obtained by a whole pattern refinement method. The calculated lattice parameters are illustrated in Fig. 2. The lattice constant a, c and cell volume V, for the doped samples increase as compared to those of the undoped sample, indicating an expansion of Li^+ pathway in the doped samples. Fig. 2b shows that the lattice constant c increases from 14.2359(2) Å (x = 0) to

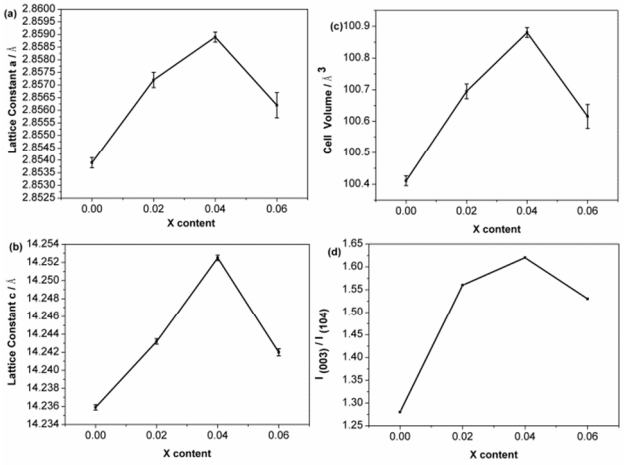

Fig.2 (a) Lattice constants of a, (b) lattice constants of c, (c) cell volume V, (d) the intensity ratio of I(003)/I(104) for all the samples.

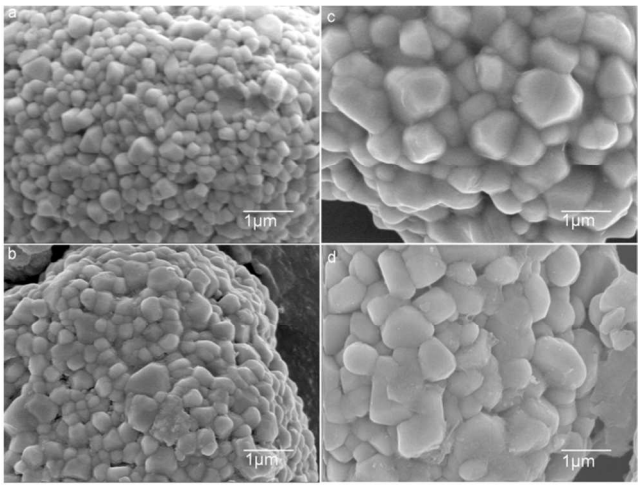

Fig.3 SEM images of all the samples: (a) x=0, (b) x=0.02, (c) x=0.04, and (d) x=0.06.

14.2525(2) Å (x = 0.04). This is attributed to the large non-equivalent Nb^{5+} ion substitution of small Mn^{4+} ion. When x > 0.04, however, the lattice parameters decrease due to the formation of Li_3NbO_4, which suggests that the solid solubility limit of Nb in $Li[Li_{0.2}Ni_{0.2}Mn_{0.6}]O_2$ has been reached. Moreover, the diffraction peaks of these doped materials slightly shifts to lower 2θ as compared to that of the undoped material as shown in Fig. 1, which indicates that the interlayer spacing is extended after doping with niobium ion. The increase of the interlayer spacing will facilitate the diffusion of lithium-ions. On the other hand, the intensity ratio of I(003)/I(104) has been reported to be strongly associated with undesirable cation mixing of $Li(Ni_{1/3}Co_{1/3}Mn_{1/3})O_2$, which has great influence on the electrochemical performance of the cathode materials.[35] The values of the I(003)/I(104) ratio increase greatly after doping (Fig. 2d), which means the low Li^+–Ni^{2+} ion mixing in the doped samples.

The SEM images of $Li[Li_{0.2}Ni_{0.2}Mn_{0.6-x}Nb_x]O_2$ (x = 0, 0.02, 0.04, and 0.06) are shown in Fig. 3. The particles of all the samples are made up of abundant small primary grains, and the morphology of the particles changes slightly after the Nb doping. With increasing amount of Nb doping, the primary grain grows obviously owing to the promotion of crystal growth by Nb_2O_5.[36]

3.2 Electrochemical behaviours

3.2.1 The effect of niobium doping on the initial charge and discharge properties.

Fig. 4a illustrates the voltage profiles of the first cycle with 0.1C current density as the charging and discharging rate for $Li[Li_{0.2}Ni_{0.2}Mn_{0.6-x}Nb_x]O_2$ (x = 0, 0.02, 0.04, and 0.06). All the

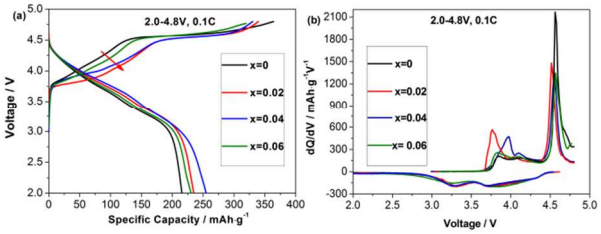

Fig.4 (a) The initial charge/discharge curves and (b) the corresponding dQ/dV curves of the 1st cycle of all the samples.

samples show similar curve shapes with a characteristic plateau around 4.5 V during charging process. According to Johnson,[3] the initial charge slope below 4.5 V corresponds to the Li^+ extraction from the $LiMO_2$ structure. The plateau around 4.5 V represents the activation of the Li_2MnO_3-type structure, which only exists in the initial cycle. During the first charge, lithium and oxygen are electrochemically extracted from the electrodes according to Eq. (1) and Eq. (2).

$$0.5Li_2MnO_3 \cdot 0.5LiMn_{0.5}Ni_{0.5}O_2 \rightarrow 0.5Li_2MnO_3 \cdot 0.5Mn_{0.5}Ni_{0.5}O_2 + 0.5Li^+ + 0.5e^- \quad \text{(Voltage below 4.5 V)} \quad (1)$$

$$0.5Li_2MnO_3 \cdot 0.5Mn_{0.5}Ni_{0.5}O_2 \rightarrow 0.5MnO_2 \cdot 0.5Mn_{0.5}Ni_{0.5}O_2 + Li^+ + e^- + 0.25O_2 \quad \text{(Voltage around 4.5 V)} \quad (2)$$

Armstrong et al.[14] have demonstrated that the formed oxygen ion vacancies would be eliminated with cationic and anionic rearrangements at the end of the initial charge, resulting in oxygen loss and structural reorganization in the Li-rich layered cathode material $Li[Li_{0.2}Ni_{0.2}Mn_{0.6}]O_2$.

The capacities of the initial charge-discharge are summarized in Table 1. It can be seen that the initial charge capacity of $Li[Li_{0.2}Ni_{0.2}Mn_{0.6}]O_2$ is 364 mAh•g^{-1}, approaching their theoretical values of 378 mAh•g^{-1}.[9] However, the initial discharge capacity increases with the increasing niobium doping (except for x=0.06). As illustrated in Table 1, the electrodes with x = 0, 0.02, 0.04, and 0.06 deliver discharge capacities of 220, 235, 254, and 231 mAh•g^{-1}, respectively.

Table 1 Initial charge/discharge capacity data of all the samples proceed at 0.1C.

Samples	Initial charge capacity(mAh/g)	Initial discharge capacity(mAh/g)	Irreversible capacity(mAh/g)	Columbic Efficiency/%
x = 0	364	221	143	61
x = 0.02	339	235	104	69
x = 0.04	330	254	82	77
x = 0.06	319	231	88	72

Furthermore, one can see clearly that there is a large difference between the charge/discharge profiles of undoped material and the Nb-doped materials (Fig. 4a). For the initial charge profiles of $Li[Li_{0.2}Ni_{0.2}Mn_{0.6-x}Nb_x]O_2$ (x = 0.02, x = 0.04 and x = 0.06), the slopes below 4.5 V shift towards the lower voltage profile (represented as arrow in Fig. 4a). It is generally accepted that the average oxidation state of Mn may remain close to Mn^{4+} throughout the first charging process in cathode material $Li[Li_{0.2}Ni_{0.2}Mn_{0.6}]O_2$ and the capacity of this sloping region (~125 mAh•g^{-1}) could be attributed to the oxidation of Ni^{2+} to Ni^{4+}.[37] The higher capacity (~175 mAh•g^{-1}) in the sloping region indicates that other charge compensation mechanisms need to be considered. This could be ascribed to the presence of Mn^{3+}, which is supposed to compensate the positive charge of the compounds in consideration of the substitution of Mn^{4+} by Nb^{5+}. Assuming that all the nickel ions are divalent as they are in

$LiMn_{0.5}Ni_{0.5}O_2$, the average manganese oxidation state varying with x in $Li[Li_{0.2}Ni_{0.2}Mn_{0.6-x}Nb_x]O_2$ compounds can be calculated as +3.97 (x = 0.02), +3.93 (x = 0.04), and +3.89 (x = 0.06).[2] Hence, it is reasonable to infer the existence of Mn3+ in the compounds.

XPS were carried out to determine the possible oxidation states of transition metal ions in the undoped sample and the sample with x = 0.04, and the corresponding spectra of pristine electrodes and charged electrodes for Mn are presented in Figure. 5a-d.

When the electrodes is charged to 4.8 V, we can find that the

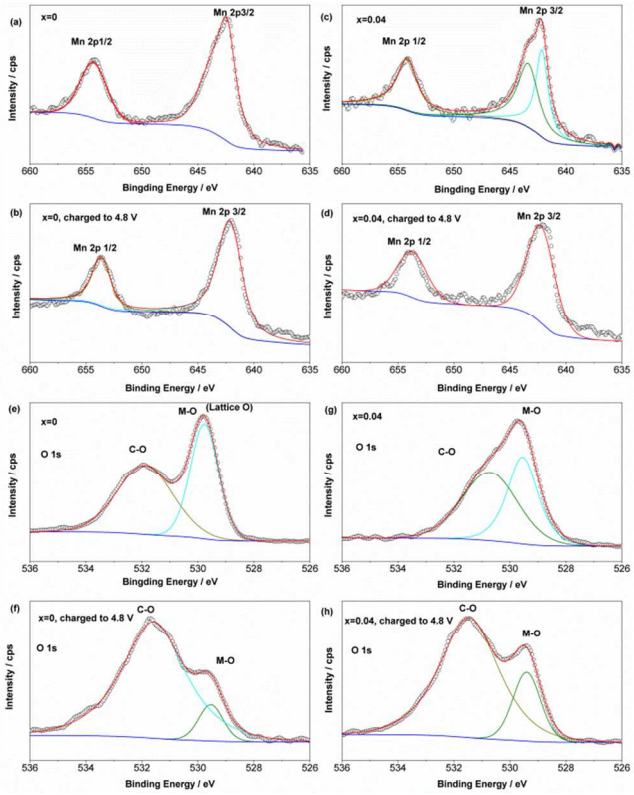

Fig.5 XPS spectra about the Mn/O: (a/e) x=0, pristine electrode, (b/f) x=0, charged to 4.8V electrode, (c/g) x=0.04, pristine electrode, and (d/h) x=0.04, charged to 4.8V electrode.

major peaks of the Mn(2p3/2) for the undoped sample and the sample with x = 0.04 centre at 642.21 eV and 642.41 eV, respectively. Binding energies (Bes) for the Mn element are in good agreement with the values reported for similar oxide cathode materials.[38,39] It can be inferred that the main oxidations state of Mn in electrodes charged to 4.8 V is 4+.[38] However, before charge, the deconvolution of the Mn(2p3/2) spectrum (Fig. 5c) of the doped sample gives two Bes for its best fit. Comparing our Bes with the values of previous report,[39] we note that the average oxidation state of Mn changes and the oxidation state of Mn ions is between +3 and +4 in the doped sample. This would give access to more electrons before the system has to oxidize oxygen ion to extract lithium-ions.

Chih Chieh et al. found that the length of the plateau region corresponded to the amount of oxygen loss from the lattice. Some factors could influence the degree of oxygen loss from the lattice, such as the binding of oxygen to the metal ions, electronegativity of the dopant ions, and the covalency of the metal–oxygen bond.[40] Therefore, the stronger Nb-O bond suppresses irreversible extraction of O^{2-} from Li_2MnO_3 component during the first cycle.

Fig. 5e-h shows the O 1s XPS spectra of the pristine electrode and the charged electrode for the undoped sample and the sample with x = 0.04, respectively. It is clear that all the asymmetric O 1s peaks are well fitted by two Gaussian-Lorentzian functions. The former broad peak at higher binding energy represent a layer of C-O type species on the surface, which could originate from the oxidation of C-contained compounds.[41] The latter peak at lower binding energy stands for M-O (M=Ni, Mn, Nb) bonds in the compound, contributing to the lattice of oxygen in the lithium-rich layered oxide.[38] It is clearly observed that there are more obvious C-O bonds and less M-O bonds, when the electrodes are initially charged to 4.8V for both samples. However, the Nb-doped sample shows more M-O bonds than that of the undoped sample, which means that Nb-doping has effects on the lattice oxygen and the Nb-doped sample has kept more lattice oxygen after the first charge.

Especially, for the initial charge profile of $Li[Li_{0.2}Ni_{0.2}Mn_{0.6-x}Nb_x]O_2$ (x = 0.06), the slope below 4.5 V shows small change as compared to the undoped sample and the plateau around 4.5 V also becomes shorter. Besides the suppression of oxygen loss, this phenomenon should be due to the fact that the formation of Li_3NbO_4 in the compounds absorbs some lithium-ions.

In contrast, the initial discharge capacity of the cathodes increases after niobium doping, resulting in lower irreversible capacity loss and higher coulombic efficiency. In the high-voltage region (4.8~3.7 V), the doping of Nb^{5+} stabilizes the layered structure, resulting in more electrochemically active Li^+ extraction/reinsertion from the electrodes.[42] In the low-voltage region (3.4~2 V), the capacity can be assigned to the reduction of Mn^{4+} to Mn^{3+}, as proposed by Yu et al.[37] However, if excessive niobium exists in the layered structure, it will form more Li_3NbO_4/Nb_2O_5 and thus reduce the amount of the active material.[31]

These results are consistent with the XRD analysis. Therefore, a small amount of Nb doping can play a positive role in the Li-rich cathode material.

In order to understand the difference of redox reaction potential in the initial cycle of all the samples, plots of dQ/dV corresponding to the 1st cycle are shown in Fig. 4b. The high oxidation peaks around 4.5 V corresponding to the plateau in Fig.4a can be attributed to the electrochemical removals of lithium and oxygen from the electrode, which is responsible for the large irreversible capacity loss.[14] The peak decreases with increasing amount of niobium, indicating that the electrochemical removal of oxygen is suppressed by niobium substitution. The two small oxidation peaks at ~3.8 V and ~4.05 V can be ascribed to the redox-reaction of Ni^{2+}/Ni^{3+} and Ni^{3+}/Ni^{4+}, respectively. However, for the sample with x = 0.02 and 0.04, the peaks around 3.8 V show broader width and have some shifting. The possible reason could be that the redox processes of Mn^{3+}/Mn^{4+} are coupled with that of Ni^{2+}/Ni^{3+}.[37] During the discharge, there are two peaks around 3.8 V and 3.3 V in the profile, as shown in Fig. 4b. The peak of ~3.8 V arises from the reduction reaction of Ni^{4+}, and the peak of ~3.3 V is probably related to the reduction of Mn^{4+} in the activated layered MnO_2 component.[37,43] On the other

hand, the sample with x = 0.06 shows a weak peak at ~3.3 V, indicating that less Mn^{4+} is reduced during the initial discharge.

3.2.2 The effect of niobium doping on cycling performance.

The cycling performances of all samples are shown in Fig. 6. All the cells are tested under a constant charge/discharge current density of 0.1C between 2.0 and 4.8 V. The discharge capacity of $Li[Li_{0.2}Ni_{0.2}Mn_{0.6}]O_2$ electrode rises at first and then decreases later, exhibiting only 83.4% of capacity retention after 100 cycles. In contrast, the Nb-doped electrodes show great improvement in cycling performance. For example, the sample with x=0.04 presents a high-capacity retention of 92.3% after 100 cycles. In

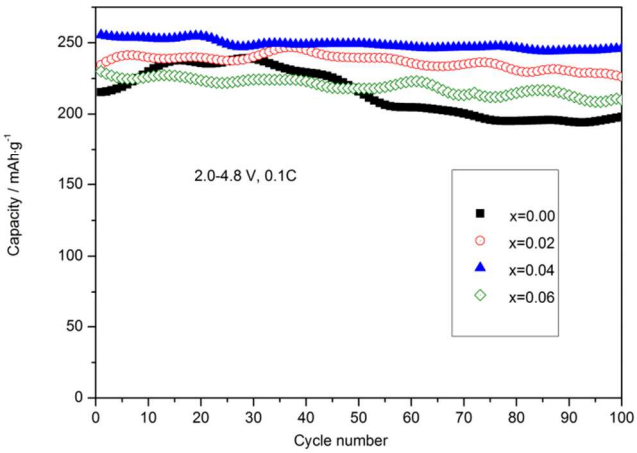

Fig.6 Cycling performance of all the samples proceeding at 0.1C rate.

addition, the samples with x=0.02 and x=0.06 also exhibit relatively small capacity loss, though they show some capacity fluctuation during the cycling. According to Hong et al.,[29] the structure of $Li[Li_{0.2}Ni_{0.2}Mn_{0.6}]O_2$ undergoes a gradual evolution upon electrochemical cycling. This structural instability results in their capacity fluctuation and capacity fading. The better cycling performance of the Nb-doped electrode could be ascribed to that doping of Nb ions into the bulk layered material can maintain the crystal structure during cycling.

To understand the differences of electrochemical behaviour between the undoped and doped samples, differential capacity analyses are performed. Herein the charge/discharge profiles of the undoped material for the 1st, 2nd, 10th, 30th and 100th cycles are shown in Fig. 7a and the corresponding capacity differential graph (dQ/dV vs. V) are plotted in Fig. 7b. Obviously, besides the disappearance of the plateau around 4.5 V, the largest change is that the activity of reaction below 3.4 V in the charge process gradually develops during the following 100 cycles. As corresponding to the capacity differential plot (Fig. 7b), the shoulders ranging from ~3.0 to ~3.4 V (as marked by arrows) during the charge process can be observed after 10 cycles and 30 cycles, while these reactions have not occurred in the first cycle. Eventually, these shoulders evolve into oxidation peak. Meanwhile, the deoxidization peaks shift largely toward lower potential, suggesting that the undoped material show increased polarization during cycling. The variation could be ascribed to that the crystal structure of the Li-rich cathode material continuously transformed from layered to spinel phase during the activation of Li_2MnO_3 component.[44] The phase transformation leads to the generation of a layered-spinel coexistent structure, corresponding to the evolution of oxidation reaction between 3.0 and 3.4 V, which explains the increase in capacity during the first few cycles in the lithium-ion batteries.[29] However, the capacity gradually decreases during the following cycles. One reason is lattice break-up and formation of porosity, which are clearly observed in the Li-rich cathode material after almost complete activation of Li_2MnO_3 component.[44] In addition, the HF in the electrolyte accelerates Mn dissolution from the spinel phase.[45]

In comparison, the charge/discharge voltage profiles for the Nb-doped electrodes exhibit much more stability during cycling, as presented in Fig. 7c. The corresponding dQ/dV plots in Fig.7d

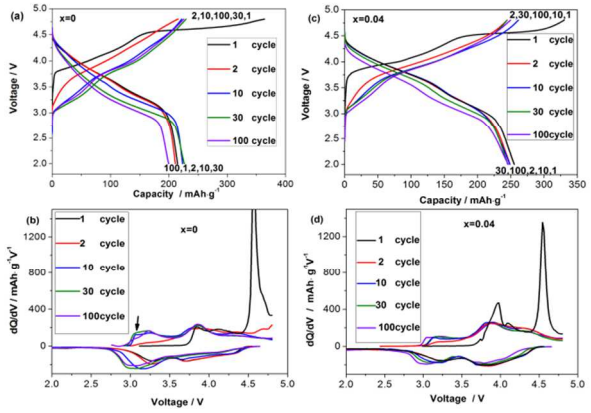

Fig.7 Charge/discharge profiles and the corresponding dQ/dV curves for $Li[Li_{0.2}Ni_{0.2}Mn_{0.6-x}Nb_x]O_2$ (x = 0 and x = 0.04).

show that the shoulders shrink after the substitution. During the cycling, the shoulders grow slowly. In other words, the redox peaks are well maintained during the lithium-ion intercalation/deintercalation in the Nb-doped electrodes. This phenomenon should be ascribed to that Nb doping in the layered material can prevent the phase transformation and stabilize the host structure of cathode materials during charge/discharge cycling.

3.2.3 The effect of niobium doping on rate capability.

One of the most crucial electrochemical characteristics of the lithium-ion battery required for electric vehicles and energy storage application is the rate capability. In order to investigate the effects of Nb doping on the rate capability, the $Li[Li_{0.2}Ni_{0.2}Mn_{0.6-x}Nb_x]O_2$ (x = 0, 0.02, 0.04, and 0.06) electrodes were charged to 4.8 V at a galvanostatic density of 20 $mA \cdot g^{-1}$ (0.1C) and discharged to 2.0 V at various current densities, viz., 0.1, 0.2, 0.5, 1, 2, and 5C. The discharge plots at various rates are presented in Fig. 8. The undoped sample $Li[Li_{0.2}Ni_{0.2}Mn_{0.6}]O_2$ shows a considerable discharge capacity at 0.1C and 0.2C rate, but it displays serious capacity fading at high rates. For example, it shows a high capacity of 225 $mA \cdot g^{-1}$ at 0.1C rate, but only 125 $mA \cdot g^{-1}$ at 1C rate. In contrast, the samples with x = 0.02, 0.04 and 0.06 have higher capacities at the same high discharge-rates. The undoped sample only delivers 125 $mAh \cdot g^{-1}$ at 1C rate while

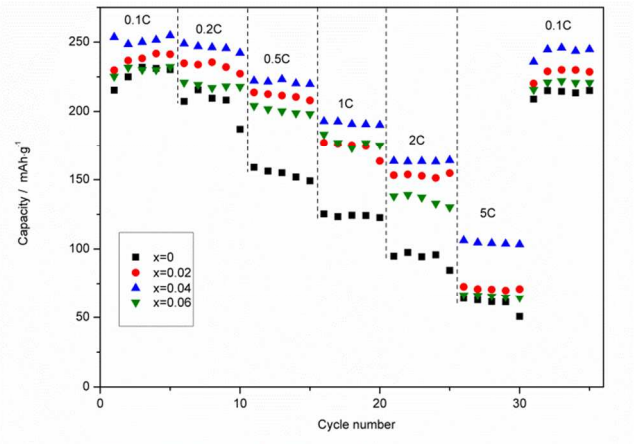

Fig.8 The rate capability of all the samples: discharge capacities under rates of 0.1C, 0.2C, 0.5C, 1C, 2C and 5C in sequence for each 5 cycles.

the doped material (x = 0.04) is able to deliver 198 mAh•g^{-1} at the same rate. Even when the cells were discharged at a current density as high as 5C rate, the doped material (x = 0.04) can still deliver a capacity of 106 mAh•g^{-1}, almost twice times more than that of the undoped sample. All these results show that 4% Nb doping is the optimum content for the high-rate capacity of $Li[Li_{0.2}Ni_{0.2}Mn_{0.6-x}Nb_x]O_2$. The poor rate capability of the undoped sample is probably due to that the formation of spinel phase damages the layered characteristics of the R $\bar{3}$ m phase, which give rise to the migration of the transition metal ions to the lithium layers and thus block the lithium-ion fast diffusionchannel.[44] However, Nb^{5+} provides higher binding energy to the oxygen sheets of the layered structure[46] and stabilizes the layered structure during the delithiation. On the other hand, the large radius of Nb^{5+} can expand the Li^+ channels and facilitate fast migration of Li^+ ions.[9] These results are consistent with the expectation from previous lattice analysis.

3.2.4 EIS measurement.

Generally, the rate capability is closely related to the charge transfer reaction and Li diffusivity in the electrodes, and the electrochemical impedance spectroscopy (EIS) measurement is an effective method to investigate the involved reaction mechanisms. Fig. 9a shows the EIS in the Nyquist plane for $Li[Li_{0.2}Ni_{0.2}Mn_{0.6-x}Nb_x]O_2$ (x =0, 0.04) cells before electrochemical cycling. In the Nyquist plots, the arc always represents the process of migration of Li ions through the surface films or charge transfer between the active material and electrolyte. [47] The slope in the low frequency region refers to lithium-ion diffusion in the bulk material. [47] Before cycles, the whole cell impedance of doped material is smaller than that of the undoped material.

Fig. 9b shows the EIS of $Li[Li_{0.2}Ni_{0.2}Mn_{0.6-x}Nb_x]O_2$ (x =0, 0.04) cells after cycling for 100 times at 0.1C constant current between 2.0 and 4.8 V. Since the measurements were performed using a two-electrode cell, the impedance from the Li anode cannot be ruled out. According to La Mantia et al., [48] impedance of the Li metal becomes stochastic at current densities above 1 mA•cm^{-2}, due to the dendrite formation, and can bring contributions to the whole cell impedance measurement. However, the major contribution of the impedance should come from the cathode.[47]

After the electrochemical cycle, the Nyquist plots show one arc in the high frequency region and two arcs in the high-to-medium frequency region. One of the arcs observed in the cycled materials could come from a contribution of the Li counter electrodes, and other two arcs could result from an SEI (passive

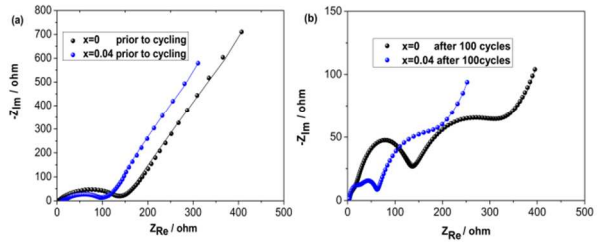

Fig. 9 (a) EIS curves of samples prior to electrochemical cycling and (b) EIS curves of $Li[Li_{0.2}Ni_{0.2}Mn_{0.6-x}Nb_x]O_2$ (x = 0 and x = 0.04) after 100 cycles, as well as (c) the equivalent circuit used to fit the measured spectra.

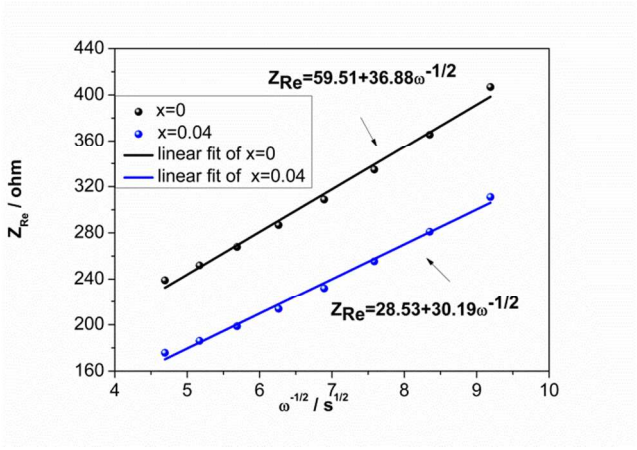

Fig. 10 Caption Plots of Z_{Re} vs. $\omega^{-1/2}$of $Li[Li_{0.2}Ni_{0.2}Mn_{0.6-x}Nb_x]O_2$ (x = 0 and x = 0.04) prior to electrochemical cycling.

solid electrolyte interface) layer and a charge transfer. [49] During the charge/discharge process, the degradation of electrode surface caused by the massive SEI film formation and the modification of surface structure associated with lattice rearrangement lead to the variation of charge transfer impedance and the SEI film impedance.[47] Thus, these arcs related to the surface condition of lithium and cathode electrodes are different from that of a fresh cell, and become larger with increasing cycle number. But it is risky to assign particular arcs to certain physical phenomena when Li foil served as both counter and reference electrodes during the EIS measurements. Therefore, we cannot precisely fit the experimental data to a certain model. But the whole cell impedance is decreasing clearly on doping and this observation is in line with the electrochemical behaviour of the studied materials. However, further investigation of their reaction mechanisms is needed.

On the other hand, the lithium ion diffusion coefficient in the electrode can be determined by applying the Fick's second law of diffusion. After a series of assumptions and simplifications, the equation for D_{Li} can be calculated by EIS parameters as Eq.(3):

$$D_{Li} = 0.5[(-dE/dx)\cdot V_m/FA\sigma_w]^2, \tau << L^2/2D_{Li} \quad (3)$$

F represents the Faraday constant, A is the surface area of the electrode, σ_w is the Warburg coefficient, V_m refers to the molar

volume of the compound, dE/dx is determined from the galvanostatic titration curve, τ is the diffusion time, and L is the finite length of the diffusion process.[50] σ_w can be determined by the slope of the Z_{Re} vs. $\omega^{-1/2}$ plots. As shown in Fig. 10, the slope of the undoped sample is larger than that of the doped sample (x = 0.4). As σ_w^2 is inversely proportional to D_{Li}, it can reflect the trend of change for D_{Li}. Therefore, the doped sample exhibits higher mobility of Li-ion diffusion in the solid phase than that of the undoped sample.

Anyway, the above results and discussions confirmed that the improvement of the Li^+ ion diffusion in the solid phase and structure stability are responsible for the better rate capability of the doped materials.

4 Conclusions

The Li-rich layered cathode materials, $Li[Li_{0.2}Ni_{0.2}Mn_{0.6-x}Nb_x]O_2$ (x = 0, 0.02, 0.04, and 0.06) were successfully synthesized by co-precipitation and solid-state reaction methods. The effects of niobium doping on the microstructure and electrochemical properties were investigated. A suitable amount of Nb^{5+} substitution for Mn^{4+} in the cathode material $Li[Li_{0.2}Ni_{0.2}Mn_{0.6}]O_2$ has great improvements in initial columbic efficiency, cycling ability and rate capability. Among those electrodes, 4% is the optimum content of Nb doping for the Li-rich cathode material $Li[Li_{0.2}Ni_{0.2}Mn_{0.6-x}Nb_x]O_2$ which shows the best electrochemical performances. The differential capacity curve and the EIS spectra were discussed to illustrate the mechanism of the improvements. All the electrochemical property enhancement of the Nb-doped materials can be attributed to three reasons.

i. The strong Nb–O bond can decrease the oxygen loss and maintain more Li^+ with electrochemically active, resulting in higher coulombic efficiency.

ii. The suppression of layered-to-spinel phase transformation by Nb^{5+} doping reduces the increase of charge transfer resistance and stabilizes the host layered structure during the electrochemical cycling, resulting in better cycling ability.

iii. The relatively large radius of Nb^{5+} can expand the Li^+ channels to facilitate fast migration of Li^+, resulting in superior rate capability.

This material may benefit the development of advanced lithium-ion batteries that meet the electric vehicle and the renewable energy storage requirements.

Acknowledgements

Financial support from the national natural science foundation of China (No.11174292, No.11374306, No.51202252, and No. 10904144) is gratefully acknowledged.

References

1 B.-S. Jin, K.-H. Ha, J.-H. Jeong, H.-S. Kim, C.-H. Doh, S.-I. Moon, Physica Scripta, T139 (2010) 014044.
2 C.S. Johnson, J.S. Kim, C. Lefief, N. Li, J.T. Vaughey, M.M. Thackeray, Electrochemistry Communications, 6 (2004) 1085-1091.
3 C.S. Johnson, N. Li, C. Lefief, M.M. Thackeray, Electrochemistry Communications, 9 (2007) 787-795.
4 C.S. Johnson, N. Li, C. Lefief, J.T. Vaughey, M.M. Thackeray, Chemistry of Materials, 20 (2008) 6095-6106.
5 J. Liu, B. Reeja-Jayan, A. Manthiram, The Journal of Physical Chemistry C, 114 (2010) 9528-9533.
6 S.K. Martha, J. Nanda, Y. Kim, R.R. Unocic, S. Pannala, N.J. Dudney, Journal of Materials Chemistry A, 1 (2013) 5587.
7 S. Park, S. Kang, C. Johnson, K. Amine, M. Thackeray, Electrochemistry Communications, 9 (2007) 262-268.
8 S.J. Shi, J.P. Tu, Y.Y. Tang, X.Y. Liu, Y.Q. Zhang, X.L. Wang, C.D. Gu, Electrochimica Acta, 88 (2013) 671-679.
9 B. Song, M.O. Lai, L. Lu, Electrochimica Acta, 80 (2012) 187-195.
10 M.M. Thackeray, C.S. Johnson, J.T. Vaughey, H.N. Li, Journal of Materials Chemistry, 15 (2005) 2257.
11 Q.Y. Wang, J. Liu, A.V. Murugan, A. Manthiram, Journal of Materials Chemistry, 19 (2009) 4965.
12 H. Yu, H. Zhou, The Journal of Physical Chemistry Letters, 4 (2013) 1268-1280.
13 Z. Lu, Dahn, J. R., Journal of The Elect rochemical Societ y, 149(2002) A815.
14 A.R. Armstrong, M. Holzapfel, P. Novák, C.S. Johnson, S.H. Kang, M.M. Thackeray, P.G. Bruce, Journal of the American Chemical Society, 128 (2006) 8694-8698.
15 R. Guo, P. Shi, X. Cheng, L. Sun, Electrochimica Acta, 54 (2009) 5796-5803.
16 H. Deng, I. Belharouak, C.S. Yoon, Y.K. Sun, K. Amine, Journal of The Electrochemical Society, 157 (2010) A1035.
17 J. Liu, A. Manthiram, Journal of Materials Chemistry, 20 (2010) 3961.
18 J. Liu, Q. Wang, B. Reeja-Jayan, A. Manthiram, Electrochemistry Communications, 12 (2010) 750-753.
19 J. Liu, H. Chen, J. Xie, Z. Sun, N. Wu, B. Wu, Journal of Power Sources, 251 (2014) 208-214.
20 D. Wang, I. Belharouak, G.M. Koenig, G. Zhou, K. Amine, Journal of Materials Chemistry, 21 (2011) 9290.
21 Y. Sun, Y. Xia, H. Noguchi, Journal of Power Sources, 159 (2006) 1377-1382.
22 L.F. Jiao, M. Zhang, H.T. Yuan, M. Zhao, J. Guo, W. Wang, X.D. Zhou, Y.M. Wang, Journal of Power Sources, 167 (2007) 178-184.
23 F.A. Amaral, N. Bocchi, R.F. Brocenschi, S.R. Biaggio, R.C. Rocha-Filho, Journal of Power Sources, 195 (2010) 3293-3299.
24 J. Zheng, X. Wu, Y. Yang, Electrochimica Acta, 105 (2013) 200-208.
25 H. Li, L.-Z. Fan, Electrochimica Acta, 113 (2013) 407-411.
26 J. Kim, B.H. Kim, Y.H. Baik, P.K. Chang, H.S. Park, K. Amine, Journal of Power Sources, 158 (2006) 641-645.
27 K. Amine, Z. Chen, S.H. Kang, Journal of Fluorine Chemistry, 128 (2007) 263-268.
28 J. Hong, D.-H. Seo, S.-W. Kim, H. Gwon, S.-T. Oh, K. Kang, Journal of Materials Chemistry, 20 (2010) 10179.
29 F. Zhou, W.B. Luo, X.M. Zhao, J.R. Dahn, Journal of the Electrochemical Society, 156 (2009) A917-A920.
30 N.A. Lange, J.A. Dean, Lange's Handbook of Chemistry, McGraw-Hill, 1973.
31 N. Li, R. An, Y. Su, F. Wu, L. Bao, L. Chen, Y. Zheng, H. Shou, S. Chen, Journal of Materials Chemistry A, 1 (2013) 9760.
32 J. Bréger, M. Jiang, N. Dupré, Y.S. Meng, Y. Shao-Horn, G. Ceder, C.P. Grey, Journal of Solid State Chemistry, 178 (2005) 2575-2585.
33 C.H. Lei, J.G. Wen, M. Sardela, J. Bareño, I. Petrov, S.H. Kang, D.P. Abraham, Journal of Materials Science, 44 (2009) 5579-5587.
34 A. Boulineau, L. Simonin, J.-F. Colin, E. Canévet, L. Daniel, S. Patoux, Chemistry of Materials, 24 (2012) 3558-3566.
35 D.D. MacNeil, Z. Lu, J.R. Dahn, Journal of The Electrochemical Society, 149 (2002) A1332.
36 D. Wang, Y. Huang, Z. Huo, L. Chen, Electrochimica Acta, 107 (2013) 461-466.
37 X. Yu, Y. Lyu, L. Gu, H. Wu, S.-M. Bak, Y. Zhou, K. Amine, S.N. Ehrlich, H. Li, K.-W. Nam, X.-Q. Yang, Advanced Energy Materials, 4 (2014) 1300950.
38 C. Gan, H. Zhan, X. Hu, Y. Zhou, Electrochemistry Communications, 7 (2005) 1318-1322.
39 K.M. Shaju, G.V. Subba Rao, B.V.R. Chowdari. Electrochimica Acta 48 (2002) 145-151.

40 C.-C. Wang, A. Manthiram, Journal of Materials Chemistry A, 1 (2013) 10209.
41 B. Qiu, J. Wang, Y. Xia, Z. Wei, S. Han, Z. Liu, ACS applied materials & interfaces, 6 (2014) 9185-9193.
42 Z.Q. Deng, A. Manthiram, The Journal of Physical Chemistry C, 115 (2011) 7097-7103.
43 H. Yu, H. Kim, Y. Wang, P. He, D. Asakura, Y. Nakamura, H. Zhou, Physical chemistry chemical physics : PCCP, 14 (2012) 6584-6595.
44 M. Gu, I. Belharouak, J. Zheng, H. Wu, J. Xiao, A. Genc, K. Amine, S. Thevuthasan, D.R. Baer, J.-G. Zhang, N.D. Browning, J. Liu, C. Wang, ACS Nano, 7 (2012) 760-767.
45 L. Yang, M. Takahashi, B. Wang, Electrochimica Acta, 51 (2006) 3228-3234.
46 M.M. Thackeray, S.-H. Kang, C.S. Johnson, J.T. Vaughey, R. Benedek, S.A. Hackney, Journal of Materials Chemistry, 17 (2007) 3112.
47 Z. Li, F. Du, Y. Wei et al. J. Phys. Chem. C, 114 (2010) 22751–22757.
48 F. La Mantia, C. D. Wessells, H. D. Deshazer, Y. Cui, Electrochemistry Communications, 31 (2013) 141-144.
49 M. D Levi and D. Aurbach, J. Phys. Chem. B, 108(2004), 11693-11703.
50 B.N.P. D. Zhang, R.E. White, Journal of Power Sources, 76 (1998) 81-90.

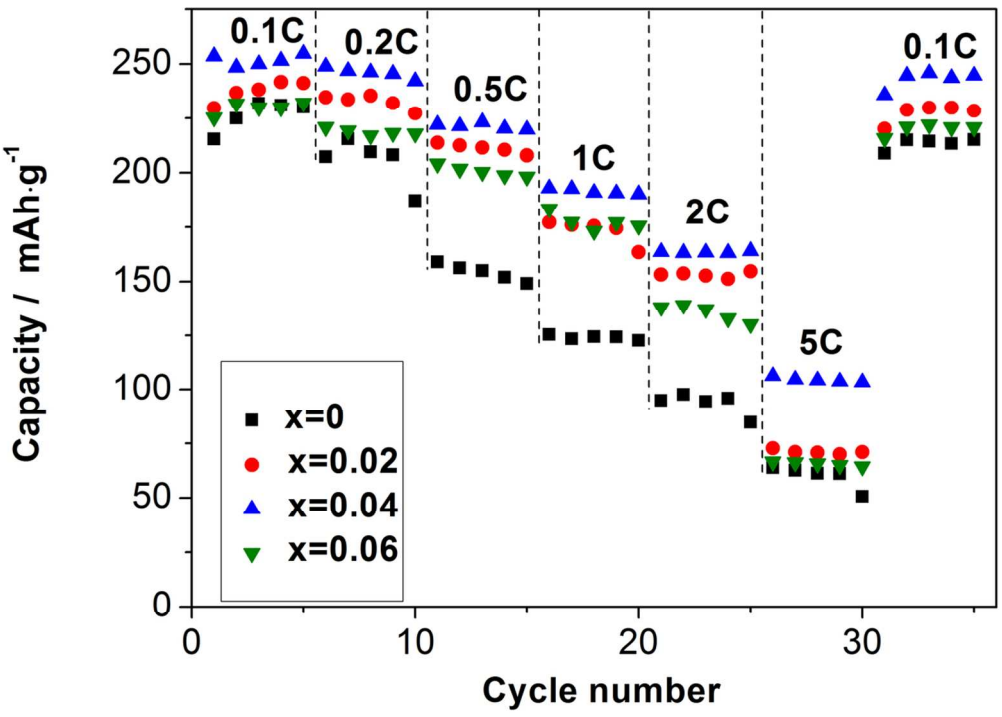

Upon Nb doping, the electrochemical properties of the Li-rich cathode material are significantly enhanced.
109x77mm (300 x 300 DPI)